Green Chemistry

PAPER

View Article Online
View Journal | View Issue

Cite this: *Green Chem.*, 2024, **26**, 10593

A biphase coupled cathode enables all-organic rocking-chair lithium ion batteries based on crystalline AB-stacked covalent triazine-based frameworks†

Xiaorong Yan,[a] Guoqing Zhao,[a] Chuanguang Wu,[a] Yujie Dai,[b] Jiakui Xiong,[b] Xinyu Wang,[b] Haiping Yu,[b] Zhihui Wang,[a] Rui Li,[b] Jingru Liu,[b] Mingjun Hu *[a] and Jun Yang*[b,c]

Organic compounds can solve many problems that lithium ion batteries currently face, such as the unsustainability and limited capacity of inorganic electrodes, due to their abundance, renewability and designability. As a kind of electroactive porous polymer, covalent triazine-based frameworks (CTFs) have shown good potential in energy storage. However, their synthesis usually requires high reaction temperature and a long reaction time or employs toxic organic reagents, resulting in uncontrollable structures, high synthesis cost and negative environmental impact. Herein, an $AlCl_3$–NaCl–KCl ternary molten salt system with a low eutectic point (~93 °C) was used for the first time for the synthesis of CTFs, and products with good crystallinity and an AB stacking structure were prepared even at 180 °C, the lowest temperature reported for the synthesis of CTFs in molten salt. Electrochemical tests further indicated that AB-stacked CTFs exhibited better electrochemical performance than the AA-stacked one and could behave as both the cathode and anode of Li-ion batteries. As a consequence, a rocking-chair full cell composed of the CTFs@Li_3PO_4 cathode and a CTF-based anode had been assembled with an initial discharge specific capacity of 101.2 mA h g^{-1} at 0.2 A g^{-1}. *Ex situ* FTIR and XPS tests revealed the reversible Li^+ insertion/extraction at C=N of triazine rings and C=C of cyclohexadiene rings for the anode and the synergistic lithium storage of triazine rings and Li_3PO_4 based on *in situ* p-type doping/dedoping of CTFs in the cathode. The concept of a biphase coupled cathode (BPCC) that combines p-type organic molecules and lithium salts for designing a rocking-chair all-organic lithium ion battery will inspire the study of high-energy organic lithium ion batteries beyond dual-ion batteries and open a new avenue for organic energy storage.

Received 13th July 2024,
Accepted 9th September 2024

DOI: 10.1039/d4gc03426k

rsc.li/greenchem

1. Introduction

Global environmental problems are growing extremely serious owing to the increased energy demand and the abuse of fossil fuels, which has sparked a broad and in-depth search for renewable energy technologies to address the severe energy crisis.[1] Three effective approaches for achieving efficient electrochemical energy storage are lithium-ion batteries, supercapacitors, and electrocatalytic decomposition of water.[1] Lithium-ion batteries have attained considerable commercial success in the electric vehicle and portable electronics markets due to their high energy and power density, acceptable safety, and environmental compatibility.[2] However, the traditional metal-based inorganic compounds, such as $LiCoO_2$, $LiNi_{0.8}Co_{0.1}Mn_{0.1}O_2$ (NCM-811), $Li_4Ti_5O_{12}$, *etc.*, used as electrode materials face a cascade of problems, such as limited capacity, insufficient resources, growing cost, high carbon footprint, and so on, hindering the further development of lithium-ion batteries. An efficient solution to this issue is to develop low-carbon and Earth abundant electrode materials for lithium-ion batteries. Owing to their availability, affordability, adaptability, benignity to the environment, *etc.*, organic compounds based on naturally abundant elements (such as C, H, O, N, and S) are drawing more and more attention in the energy storage field.[3–6]

[a]*School of Materials Science and Engineering, Beihang University, Beijing 100191, China. E-mail: mingjunhu@buaa.edu.cn*
[b]*Beijing Institute of Nanoenergy & Nanosystems, Chinese Academy of Sciences, Beijing 101400, China. E-mail: yangjun@binn.cas.cn*
[c]*Shensi Lab, Shenzhen Institute for Advanced Study, University of Electronic Science and Technology of China, Shenzhen 518110, China*
† Electronic supplementary information (ESI) available. See DOI: https://doi.org/10.1039/d4gc03426k

Covalent organic frameworks (COFs) materials are an emerging class of crystalline and porous polymeric materials that allow the precise integration of structural units with redox activity into two- or three-dimensional (2D or 3D) polymeric frameworks with long-range ordered backbones and nanopores.[7] Currently, the most typical design idea is the introduction of unsaturated polar organic groups (radicals, C═O, C═N, N═N) into COFs as redox centers to increase the specific capacity of lithium-ion batteries.[8] However, although COFs have the aforementioned benefits, their development is still constrained mainly attributed to high synthetic cost, where expensive organic reagents, high reaction temperature, a long reaction time and multi-step processes are usually involved.[3] Covalent triazine-based frameworks (CTFs) are a kind of porous polymer containing triazine rings and have been widely used in a variety of energy storage devices due to their rich active sites, large specific surface area, good durability, and decent electrical conductivity.[9] Most CTFs belonged to bipolar molecules and could store charges through both p-type and n-type doping of triazine rings.[9,10] Recently, several research teams have investigated the electrochemical performances of CTFs and found that they could behave as both the cathodes and anodes of lithium-ion batteries. For example, Cai *et al.* studied the performance of a CTF with an AA stacking structure as an anode for lithium-ion batteries and achieved a specific capacity of 570 mA h g^{-1} at a current density of 100 mA g^{-1} after 50 cycles.[11] When utilized as the cathode of Li-ion batteries, the CTF exhibited substantially low reversible capacities (23 ± 10 mA h g^{-1} at 0.1 A g^{-1} after the 100th cycle) according to the research by See *et al.*[12] It was also found that by modifying the CTF materials, such as exfoliation and doping with F atoms, the electrochemical performance of CTFs could be further enhanced,[13] implying that not only the molecular structure but also the stacking mode affected the materials' electrochemical behaviors.

However, although CTFs have shown great application potential in energy storage, currently most CTFs are synthesized in organic solvents by using a strong acid, such as trifluoromethanesulfonic acid,[14–16] as the catalyst, or through the $ZnCl_2$-based high-temperature molten salt method. In these two methods, solution-based synthesis usually requires the use of a toxic organic solvent that is not friendly to the human body and the environment and the $ZnCl_2$-based molten salt method needs a high reaction temperature to enable the melting of $ZnCl_2$ (293 °C), which easily incurs hot-working defects and the carbonization of the polymer in a long timeframe (>40 h),[17] resulting in poor structure controllability and erratic electrochemical performance (Table S1†).[18] Therefore, development of new synthetic methods for avoiding the use of toxic organic solvents as well as decreasing the reaction temperature is in high demand.

In view of the above-mentioned issues, in this work, we propose a new transition metal-free molten salt system with a low eutectic point (93 °C),[19,20] $AlCl_3$–NaCl–KCl, for the synthesis of CTFs. Different from the conventional $ZnCl_2$-based high-temperature molten salt synthetic method where AA-stacked CTFs are made above 400 °C, the $AlCl_3$–NaCl–KCl ternary molten salt system can produce crystalline AB-stacked CTFs at 180 °C, which is the reported minimum temperature for the synthesis of CTFs in the molten salt method. Furthermore, the electrochemical performances of crystalline AB-stacked CTFs as the cathode and anode of Li-ion batteries, respectively, were investigated for the first time. It was discovered that compared to the AA-stacked structure, crystalline AB-stacked CTFs could display obviously better cathode performance in Li-ion batteries. It is especially interesting that by introducing Li_3PO_4 salt into the CTFs, we prepared a lithium-containing biphase coupled cathode (BPCC) composed of Li_3PO_4 and CTFs. By pairing the composite cathode with the CTF anode, we constructed a rocking-chair all-organic lithium-ion battery. Different from conventional dual ion batteries where anions and cations in the electrolytes insert/extract into/from the cathode and anode respectively to fulfil charge and discharge,[21–23] the biphase coupled cathode can transform the (de)inserted ions in the cathode from anions to cations, enabling a complete cation-based rocking-chair battery. Consequently, the assembled battery showed an initial discharge specific capacity of 101.2 mA h g^{-1} at 0.2 A g^{-1} (the theoretical specific capacity of the CTF from p-doping is 139 mA h g^{-1}), much higher than that of a dual ion battery (48.9 mA h g^{-1}). The research results indicated that the transformation from the triazine ring to its radical cations and timely *in situ* charge compensation from phosphate groups of Li_3PO_4 in the composite cathode played a critical role in enhancing the electrochemical activity of the composite cathode. The design idea of the p-type organic cathode coupled with lithium salts to transform the (de)inserted ions from large anions into small cations can greatly improve the reaction dynamics, specific capacity and cycling stability of the cathode and thus will shed light on next-generation high energy batteries and open a brand new route for organic energy storage.

2. Results and discussion

In a typical synthesis process, $AlCl_3$–NaCl–KCl were ground into homogeneous powders in proportion to each other, and then the ground salt and 1,4-dicyanobenzene (DCB) were mixed sufficiently and heated in a sealed quartz tube in a constant-temperature oven (Fig. 1a). It was found that the cyclotrimerization reaction of the cyano groups could be well induced in the $AlCl_3$-based ternary molten salt system at 180 °C, where $AlCl_3$ acted as both the reaction medium and the Lewis acid catalyst, and NaCl and KCl helped to liquefy $AlCl_3$ at a temperature lower than its sublimation point to prevent the direct vaporization of $AlCl_3$. When only $AlCl_3$ and DCB were employed in the reaction, the powder X-ray diffraction (PXRD) result of the product was the same as that of the raw material DCB, indicating that no cyclotrimerization reaction took place, attributed to the fact that pure $AlCl_3$ would not reach the molten state below 200 °C and thus could not induce cyclotri-

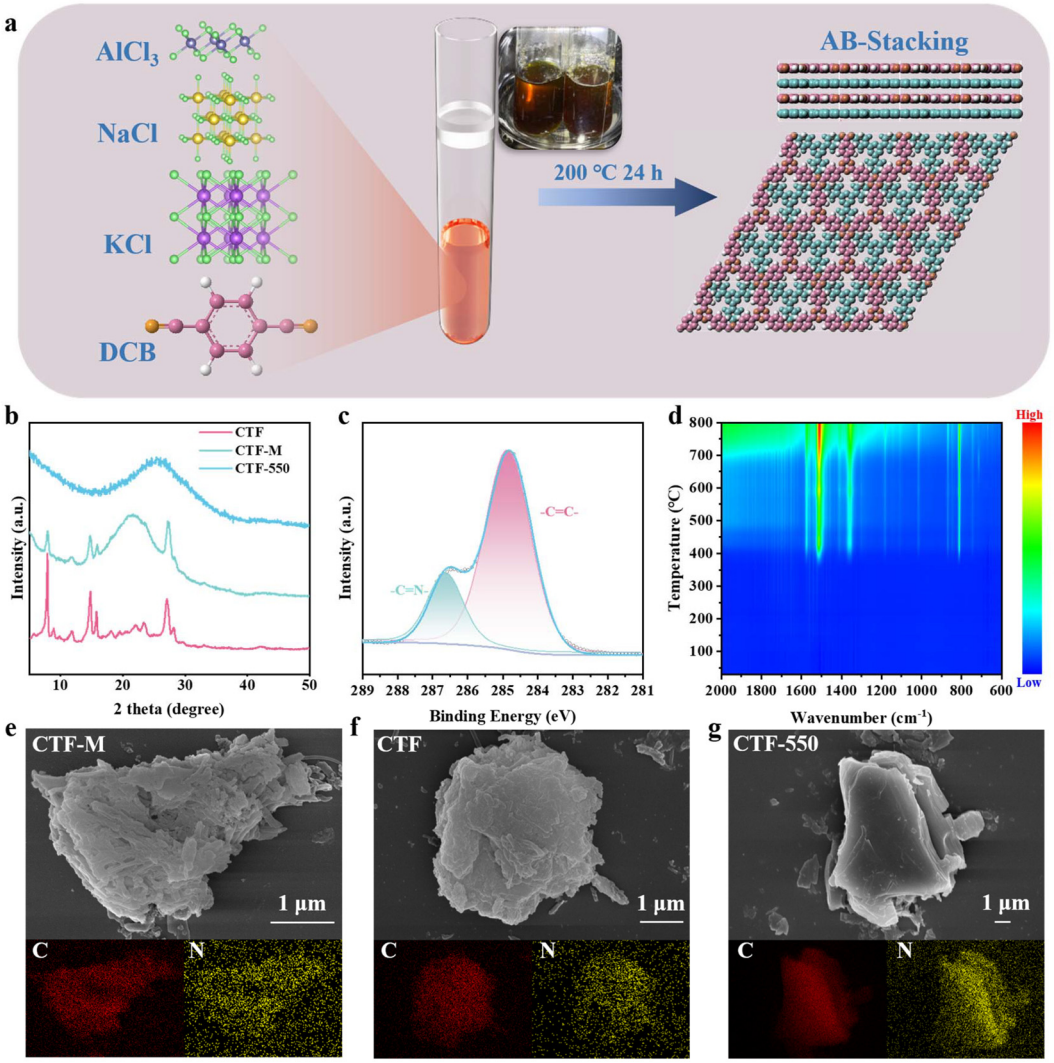

Fig. 1 (a) Illustration of the preparation process of CTFs. (b) The XRD patterns of CTF, CTF-M and CTF-550. (c) The C 1s XPS spectra of CTF. (d) The TG-FTIR spectra of CTF. The SEM images and C and N elemental mapping images of (e) CTF-M, (f) CTF, (g) CTF-550.

merization (Fig. S1a and b†). At 400 °C, although aluminum chloride was in the molten state, the product would suffer partial decomposition and carbonization, rendering an amorphous form (Fig. S1c–e†). When NaCl or KCl was added into $AlCl_3$ to construct a low-melting-point eutectic salt, crystalline CTFs were obtained. Among them, the product with the best crystallinity was obtained when the molten salt was composed of $AlCl_3$, NaCl and KCl (Fig. S2†). The XRD of the CTF demonstrated that the products were consistent with the AB stacking model (Fig. 1a), and the crystallinity was significantly influenced by the ratio of DCB to molten salt, reaction duration, and reaction temperature (Fig. S3†). By comparing the CTFs' crystallinity under a series of reaction conditions, it was found that the optimal CTF was obtained in the $AlCl_3$–NaCl–KCl system with a ratio of DCB to salts of 1 : 0.5 and a reaction time of 24 h at 200 °C (Fig. S4–S6†). To improve the electrochemical properties of the CTFs, additional ball milling post-treatment (denoted as CTF-M) and high-temperature heat treatment (denoted as CTF-T) were also carried out to increase their specific surface area and conductivity.

As shown in Fig. 1b and Fig. S7,† the PXRD pattern of the pristine CTF exhibited extremely narrow and intense peaks, indicative of their excellent crystallinity, and additional ball milling and heat treatment at 550 °C would weaken the diffraction peaks, but the heat treatment below 450 °C did not affect the crystallinity obviously (Fig. S8†). According to a previous report, the diffraction peak at 7.88° can be assigned to the $\{10\bar{1}0\}$ plane, and those peaks located at 14.77°, 15.76° and 27.05° correspond to the $\{11\bar{2}0\}$, $\{20\bar{2}0\}$ and {0002} planes, respectively.[17] The scanning electron microscopy (SEM) images showed that the CTF and CTF-M had a stacked lamellae structure, and the heat-treated CTF at 550 °C (CTF-550) appeared as an irregular block with a smooth surface. The laminated structure of CTF materials can also be observed by transmission electron microscopy (TEM) and atomic force microscopy (AFM) (Fig. S9 and S10†). The energy dispersive spectra (EDS) showed

the uniform distribution of C and N in all three CTFs (Fig. 1e–g). The chemical structure of CTFs was further analyzed by Fourier transform infrared (FT-IR) spectroscopy and X-ray photoelectron spectroscopy (XPS). As shown in Fig. S11,† the two sharp peaks at 1362 cm^{-1} and 1519 cm^{-1} in CTF and CTF-M were attributed to the C=N breathing and stretching vibrations in the triazine rings, respectively.[17] The weakening of the peak intensity at 1519 cm^{-1} in CTF-550 may be due to the escape of triazine ring-containing moieties at high temperature. The incomplete polymerization of DCB monomers or the residual oligomers may be responsible for the appearance of the peak attributed to the C≡N bond at 2231 cm^{-1}. As displayed in Fig. 1c, there are two peaks in the C 1s XPS spectra of the CTF. The sp^2 hybrid C species in the benzene rings are responsible for the peak at 284.8 eV, and the sp^2 hybrid C species in the triazine rings (–C=N–) are responsible for the peak with a higher binding energy at 286.58 eV. The formation of the triazine N (–C=N–C–) can also be seen in the N 1s XPS spectra of the CTF at 398.8 eV (Fig. S12†).[24,25]

Thermogravimetric analysis (TGA) (Fig. S13†) showed that the thermal stability of the CTF was excellent, and there was no obvious weight loss below 400 °C, which is consistent with the XRD results. From the TG-FTIR, it could be seen that the infrared spectra of the released gas above 500 °C were still the same as that of the original CTF, indicating that the weight loss at high temperature was mainly derived from the splitting of carbon–carbon bonds and the escape of CTF oligomers (Fig. 1d). The Brunauer–Emmett–Teller (BET) specific surface areas of the CTF, CTF-M, and CTF-550 were 25, 30, and 30 $m^2 g^{-1}$, respectively, according to N_2 adsorption experiments (Fig. S14†), which was consistent with previous reports.[26] Furthermore, according to the elemental analysis (EA), the ratios of carbon to nitrogen of the CTF and CTF-M were also close to the theoretical values (4 : 1), and the slightly higher carbon to nitrogen ratio of CTF-550 may be due to the slight carbonization of the material at a high temperature (Table S2†).

In order to explore the application of CTF materials in lithium-ion batteries, different CTFs were used as the cathodes and anodes of lithium-ion batteries respectively. To identify the influence of different stacking modes on the electrochemical performance of CTFs, we investigated the electrochemical performance of AB-stacked CTF, CTF-M, and AA-stacked CTF synthesized in $ZnCl_2$ molten salt (CTF-AA) as the cathode of lithium-ion batteries. The electrochemical impedance spectroscopy (EIS) results of CTF, CTF-M and CTF-AA are shown in Fig. S15,† and the Nyquist plot is constituted by a straight line at low frequency and a semicircle at high frequency, which is ascribed to the Warburg impedance and charge-transfer resistance (R_{ct}). The crystalline CTF and CTF-M showed greater Warburg impedance and R_{ct} than CTF-AA, may be owing to better ionic conductivity derived from smoother ion channels in the AA-stacked CTF. Cyclic voltammetry (CV) measurements of the CTF and CTF-M were performed at a scan rate of 5 mV s^{-1} over a voltage range of 1.5–4.5 V (*vs.* Li/Li^+) (Fig. S16†). The oxidation peaks of CTF and CTF-M at 3.6 V are ascribed to the p-type doping mechanism of the triazine rings, which was accompanied by the insertion of the anion (PF_6^-) at high voltage.[27] This gradually weakened peak intensity with the cycles should be attributed to the gradual destruction of CTF crystalline structures during cycling (Fig. S17†). Notably, the CV curves of CTF-AA did not show any obvious redox peaks, which is consistent with previous reports (Fig. S18†).[9,12]

Fig. 2a shows the rate capability of CTF, CTF-M, and CTF-AA at different current densities, and the specific capacities of CTF and CTF-M were much higher than that of CTF-AA at all current densities. The reversible discharge capacities of CTF were 129.6, 82.8, 60.1, 45.2, 34.2, 24.7 and 21.2 mA h g^{-1} at current densities of 0.1, 0.2, 0.5, 1, 2, 5 and 10 A g^{-1}, respectively. When the current density was returned to 0.1 A g^{-1} again, the specific capacity still recovered to 102.7 mA h g^{-1}. Additionally, CTF and CTF-M had better cycling stability than CTF-AA, maintaining specific capacities of 69.9 mA h g^{-1} and 83.6 mA h g^{-1} after 1000 cycles at 0.1 A g^{-1}, with capacity retention rates of 68.1% and 94.4%, respectively, while the CTF-AA only maintained a very low specific capacity of 26.4 mA h g^{-1} after 300 cycles (Fig. 2b). The excellent cycling performance of the CTF and CTF-M as the cathode may be attributed to their robust triazine-based skeleton and few defects by virtue of low-temperature $AlCl_3$-based molten salt synthesis. Even when the current density was increased to 1 A g^{-1}, the CTF could still provide a reversible specific capacity of 76.5 mA h g^{-1} and show a capacity retention of 71.1% after 5000 cycles (Fig. 2c), which was much higher than that of CTF-AA (42.5 mA h g^{-1} and 32.9%, respectively). By comparing the EIS before and after cycling of CTF, CTF-M, and CTF-AA, it was found that the R_{ct} value after cycling of CTF and CTF-M with AB stacking structure were smaller than the initial R_{ct}, whereas the R_{ct} after cycling of CTF-AA was larger than the initial R_{ct} (Fig. S19†), indicating that the low-crystalline AA-stacked CTFs may suffer more serious damage during charge and discharge at high potentials due to more defects. In addition, the R_{ct} value of CTF-M after cycling was much smaller than that of CTF and CTF-AA, consistent with its better electrochemical performance (Fig. S20†). Compared with CTF-M, CTF showed a significant capacity decay in the pre-cycling period, followed by a gradual increase, which may be attributed to the fact that CTF has a slow activation process as a result of a larger particle size, whereas CTF-M did not show this process due to its more fragmented and delaminated structure, which makes it easier to be infiltrated by the electrolyte.

In order to further understand the energy storage mechanism of the material, *ex situ* FT-IR spectroscopy and *ex situ* XPS were performed for CTF electrodes as the cathode at different charge/discharge stages. Fig. 2d shows the charge/discharge curves of the CTF electrode at 0.1 A g^{-1} between 1.5 and 4.5 V. The *ex situ* FT-IR spectra in Fig. 2e show that the vibrational peaks of the C=N bonds at 1512 cm^{-1} and 1358 cm^{-1} gradually weakened during the discharge process and then gradually increased during the charging process,

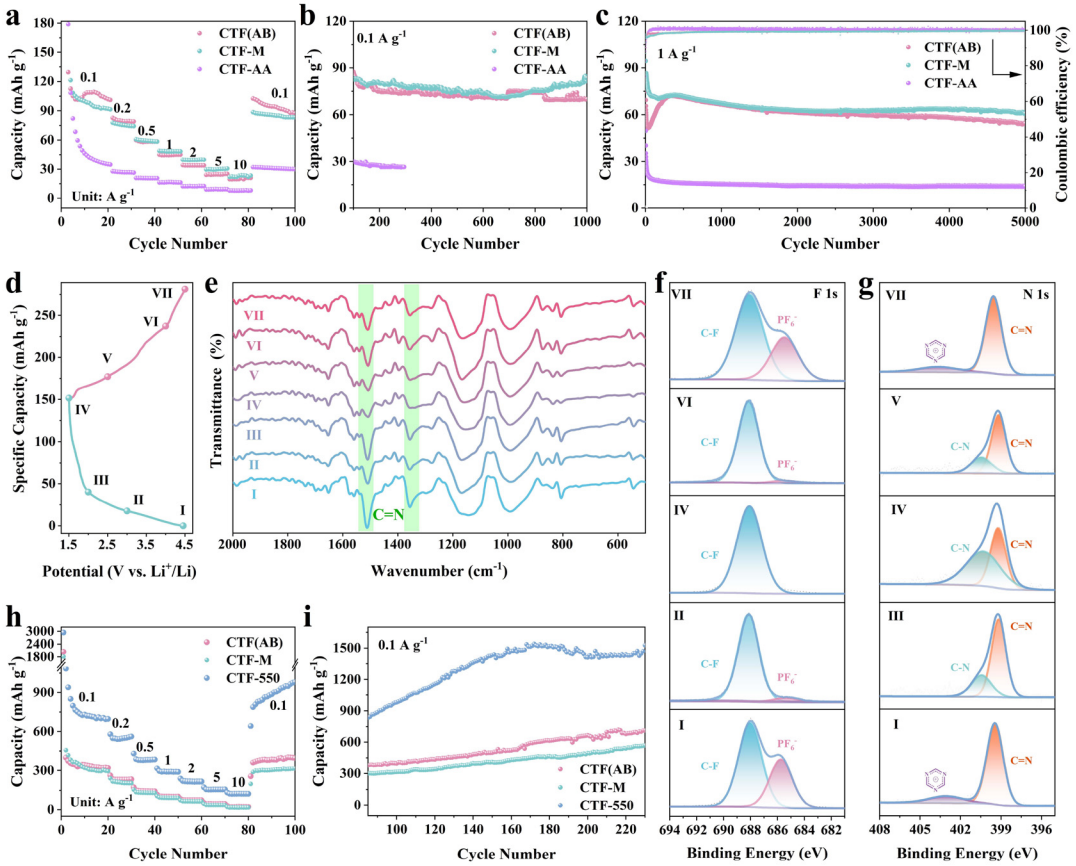

Fig. 2 (a) Rate performance of CTF, CTF-M, and CTF-AA as the cathode at various current densities. (b) Cycling performance of CTF, CTF-M, and CTF-AA as the cathode at 0.1 A g^{-1}. (c) Long-term cycling stability of CTF, CTF-M, and CTF-AA as the cathode at 1 A g^{-1}. *Ex situ* characterization of the CTF electrode as the cathode at different discharge and charge states: (d) charge/discharge curves; (e) FT-IR spectra of CTF; (f) F 1s XPS spectra of CTF; (g) N 1s XPS spectra of CTF. (h) Rate performance of CTF, CTF-M, and CTF-550 as the anode in the voltage range of 0.005–3 V at various current densities. (i) Cycling performance of CTF, CTF-M, and CTF-550 as the anode at 0.1 A g^{-1}.

corresponding to the lithiation and delithiation processes, respectively, indicating that the triazine ring underwent reversible and stable electrochemical reactions during the charging and discharging processes.[10] The XPS results of the pristine CTF electrode are shown in Fig. S21,† and the peak at 688.1 eV in the F 1s spectrum was attributed to the covalent bond C–F of PVDF,[28] while the peak at 399.58 eV in the N 1s spectrum was attributed to the C=N bond of CTF.[10] As shown in Fig. 2f, only C–F peaks appeared in the F 1s spectrum of the electrode when discharged to 1.5 V. The peak at 685.88 eV attributed to PF_6^- appeared during charging, and the PF_6^- peaks were continuously strengthened with charging and gradually weakened during discharging, which corresponded to the p-type doping mechanism of CTF materials.[29–33] Similarly, in Fig. 2g, it can be seen that a peak at 400.3 eV appeared in the N 1s spectrum of the electrode attributed to the C–N bond when discharged to 1.5 V, which corresponded to the n-type energy storage mechanism of the CTF, whereas as charging proceeded, the peaks of C–N gradually weakened and a peak appeared at about 403 eV corresponding to the triazine radical cation, which was also in agreement with the p-type doping energy storage mechanism of the CTF.[23,27,34–37] By combining the *ex situ* FT-IR spectra and *ex situ* XPS results, it was demonstrated that the triazine ring could achieve n-type doping/dedoping with reversible Li^+ insertion/extraction at low voltage, and could also realize p-type doping/dedoping by combining with PF_6^- anions at high voltage to maintain good electrochemical performance. To further confirm the energy storage process, the lithiation process of the CTF was calculated by density functional theory (DFT). The CTF as shown in Fig. S22† has a low LUMO energy level (−2.75 eV), indicating that the CTF has great electron affinity and a high reduction potential. Meanwhile, it showed a LUMO–HOMO energy gap of 4.14 eV, more close to a non-conductor.[11] From the MESP diagram in Fig. S23,† the lowest electrostatic potential was found near the N atoms of the triazine rings. The region with the most negative electrostatic potential would have a stronger interaction with Li^+ and would bind with Li^+ more easily. According to theoretical calculations and experimental results, the high specific capacity of the CTF was mainly attributed to the reversible charge storage of the triazine rings.[38]

The Nyquist plots of CTF, CTF-M and CTF-550 as anodes are shown in Fig. S24.† The slope line was related to the lithium ion diffusion impedance, and the slope of CTF-550 was higher than

that of CTF and CTF-M, indicating that it has better lithium ion transport kinetics.[39] As shown in Fig. S25,† CV curves were also obtained at a scan rate of 5 mV s^{-1} over the voltage range of 0.005 V–3.0 V. It is noteworthy that a strong reduction peak was observed at 0.53 V in the first cycle, which was an irreversible electrochemical process due to the formation of the solid electrolyte interface (SEI) layer. After the first several cycles, the curves of CTF-550 almost completely overlapped compared to CTF and CTF-M, demonstrating good cycle reversibility and stability. Fig. 2h presents the rate capability of CTF, CTF-M and CTF-550 at different current densities, and CTF-550 showed much higher specific capacity than CTF and CTF-M. As can be seen, the initial discharge capacity of CTF-550 reached 2944.7 mA h g^{-1} at 0.1 A g^{-1}, much higher than those of CTF (1814.9 mA h g^{-1}) and CTF-M (2038.2 mA h g^{-1}). CTF-550 exhibited highly reversible average discharge specific capacities of 552.1, 387.5, 293.0, 218.9, 158.0, and 124.3 mA h g^{-1} at 0.2, 0.5, 1, 2, 5 and 10 A g^{-1}, respectively. To further evaluate the cycling stability, the long-term cycling performance of these electrodes was measured at 0.1 A g^{-1} and 1 A g^{-1} and is shown in Fig. 2i and Fig. S26.† After a cascade of charge/discharge cycles at different current densities, CTF-550 showed a higher reversible capacity of 642.8 mA h g^{-1} when the current density was back to 0.1 A g^{-1} again, surpassing CTF (255.5 mA h g^{-1}) and CTF-M (198.7 mA h g^{-1}). The specific capacities of all three samples showed a gradual increase, which should be attributed to the gradual activation of organic electrodes during cycling.[40] After 168 cycles, we can see that the capacity of CTF-550 has increased to 1535.4 mA h g^{-1}, CTF to 538.3 mA h g^{-1}, and CTF-M to 444.3 mA h g^{-1} (Fig. 2i). At a current density of 1 A g^{-1}, CTF-550 exhibited a more pronounced capacity decay in the initial cycles and a capacity increase after the 40th cycle (Fig. S26†). The steady capacity increase in the subsequent ~700 cycles could be attributed to the gradual utilization of the active sites due to electrolyte penetration after deep cycling. In contrast, the CTF-AA had a lower capacity and did not show significant capacity growth (Fig. S27†) maybe due to less crystalline structure and faster activation process. In addition, the *ex situ* FT-IR spectroscopy of CTF-550 as an anode in different charging and discharging states was also performed. Similar results to those as the cathode can be observed in Fig. S30,† except that the change in peak intensity at 808 cm^{-1} can be attributed to the transformation from C=C of cyclohexadiene rings to Li–C–C–Li at low potentials. The utilization of carbon–carbon unsaturated bonds as the active sites results in a much higher specific capacity of the CTF anode than that as the cathode.[40–43]

Considering that CTF materials have good performance both as anode and cathode of lithium-ion batteries, we chose CTF-M and CTF-550 as the cathode and anode of lithium-ion batteries respectively and assembled a dual ion cell (CTF-M//CTF-550). Since CTF materials show poor conductivity, the effect of conductive additives (ketjen black) on the performance of the dual ion cell was measured foremost. As can be seen in Fig. S31,† the capacity of CTF-M//CTF-550 gradually increased as the electrode conductivity was enhanced with the increase of the content of ketjen black in the cathode. When the weight ratio of CTF-M, ketjen black and PVDF was 4 : 5 : 1, a specific capacity of 36.3 mA h g^{-1} can be maintained after 80 cycles at 1 A g^{-1}, attributed to the fact that Li^+ and PF_6^- in the electrolyte were embedded in the anode and cathode, respectively, during the charging process. Fig. S32† shows the rate performance of the CTF-M//CTF-550 with a discharge specific capacity of 48.9 mA h g^{-1} at 0.2 A g^{-1}, consistent with the p-type doping capacity (>3.0 V)[44,45] of a CTF-M//Li half cell (Fig. S33†), but the CTF-M//CTF-550 had a significant capacity decay and unstable coulombic efficiency, may be attributed to poor reaction dynamics and reversibility of insertion/extraction of PF_6^- in the CTF-M cathode of the dual ion battery in the absence of an n-type doping process.

To avoid the insertion/extraction of large PF_6^- anions, a composite cathode CTF-M@Li_3PO_4 was designed and prepared by adding Li_3PO_4 to CTF-M (the weight ratio of CTF-M : Li_3PO_4 was 3 : 1), in which PO_4^{3-} anions with a higher charge-to-mass ratio replaced PF_6^- anions for balancing the positive charge of triazine radical cations after CTF oxidation, and Li^+ ions became the main carriers. The electrochemical performance of the CTF-M@Li_3PO_4//Li half cell was first investigated. The CV measurement of CTF-M@Li_3PO_4 (Fig. 3a) showed that the peak position of the CTF-M@Li_3PO_4 composite electrode was consistent with that of CTF-M, with an oxidized peak at 3.6 V, corresponding to the p-type doping of CTF-M. The rate performance of the CTF-M@Li_3PO_4 composite electrode and the CTF-M electrode is shown in Fig. 3b, and the charge/discharge curves of the CTF-M@Li_3PO_4 composite electrode are shown in Fig. 3d, when the weight ratio of the active materials : ketjen black : PVDF was 6 : 3 : 1. It can be seen that the CTF-M@Li_3PO_4 composite electrode performed much better, with a specific capacity of 129.6 mA h g^{-1} when the current density was returned to 0.1 A g^{-1} again (Fig. 3b), which was significantly higher than that of single CTF-M (82.4 mA h g^{-1}), and a specific capacity of 89.3 mA h g^{-1} was still maintained after 300 cycles at 0.1 A g^{-1} (Fig. 3c). To improve the electrochemical properties of the composite electrode, we further increased the ratio of ketjen black (Fig. S34†), and when the weight ratio of CTF-M, ketjen black and PVDF was 4 : 5 : 1 (Fig. 3e), the initial specific capacity of the CTF-M@Li_3PO_4 composite electrode became 255.1 mA h g^{-1} at 0.1 A g^{-1}. After a cascade of charge/discharge at higher current densities, the capacity could recover to 212.8 mA h g^{-1} when the current density was returned to 0.1 A g^{-1} again, which was much higher than that of the CTF-M electrode (147.3 mA h g^{-1}). The corresponding p-type doping capacity of the CTF-M@Li_3PO_4 composite electrode was evaluated from the discharge curve to be about 55.9 mA h g^{-1} (Fig. 3f), which was higher than that of CTF-M to be 46.5 mA h g^{-1} (Fig. S33†), indicating that the addition of Li_3PO_4 can improve both the p-type and n-type doping capacities of CTF-M.

As suggested, the work mechanism of CTF-M@Li_3PO_4 composite cathode can be considered as shown in eqn (1), in which Li_3PO_4 can provide PO_4^{3-} anions for *in situ* charge compensation during the cathode oxidation and convert the main carriers from large PF_6^- anions into small Li^+ cations, which is beneficial for improving the reaction dynamics, specific

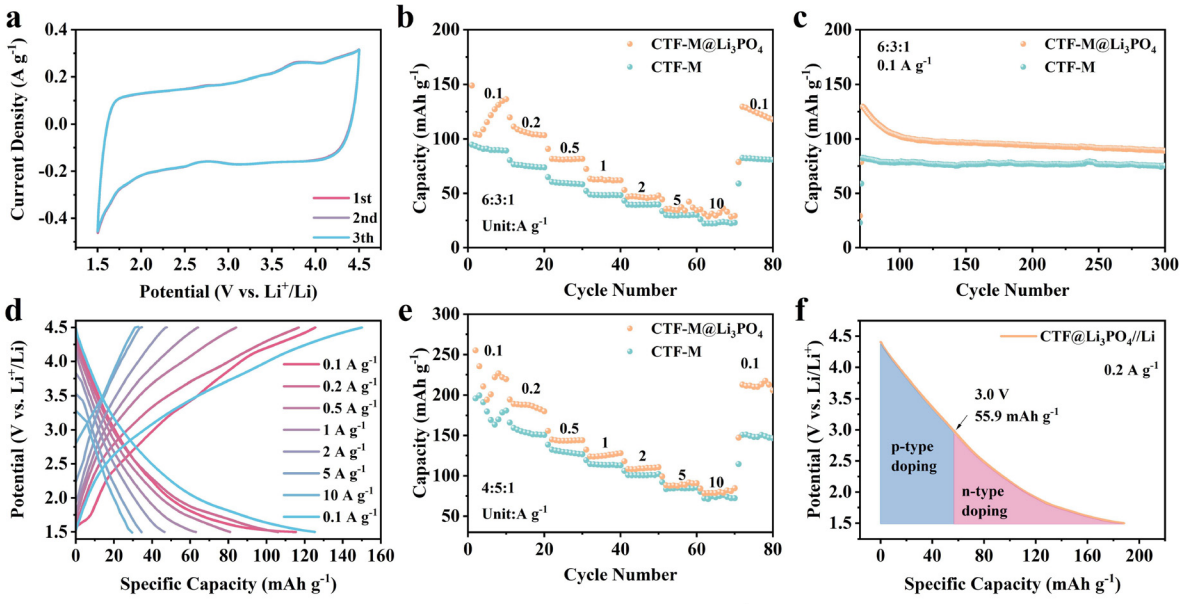

Fig. 3 (a) CV curves of CTF-M@Li_3PO_4//Li at 5 mV s^{-1}. (b) Rate performance of CTF-M and CTF-M@Li_3PO_4 as the cathode with the CTF-M, ketjen black and PVDF weight ratio of 6 : 3 : 1. (c) Cycle performance of CTF-M and CTF-M@Li_3PO_4 as the cathode with the CTF-M, ketjen black and PVDF weight ratio of 6 : 3 : 1 at 0.1 A g^{-1}. (d) Charge/discharge curves of CTF-M@Li_3PO_4//Li at various current densities. (e) Rate performance of CTF-M and CTF-M@Li_3PO_4 as the cathode with the CTF-M, ketjen black and PVDF weight ratio of 4 : 5 : 1. (f) Discharge curve of CTF-M@Li_3PO_4//Li at 0.2 A g^{-1}, and its corresponding n-type and p-type doping capacity contributions.

capacity and cycling stability. To verify the mechanism, *ex situ* XPS spectra analysis was carried out on the composite cathode at different charge/discharge stages. It can also be seen from the XPS spectra of F 1s that when CTF-M alone was used as the cathode, the peaks attributed to PF_6^- could be seen to appear in the charged state (Fig. 2f), whereas no new peaks appeared and only the peaks attributed to PVDF were seen when CTF-M@Li_3PO_4 was used as the cathode (Fig. S35†), indicating that the insertion/extraction of PF_6^- anions did not happen for the CTF-M@Li_3PO_4 cathode. It appeared that in this situation, the cathode could behave more like conventional inorganic cathodes, such as $LiFePO_4$, where Li_3PO_4 was the lithium source and p-type CTF-M played the role of Fe^{2+}, and thus convert the (de)insertion of large anions (PF_6^-) as a dual ion battery does into (de)insertion of small lithium ions (Li^+). The diffusion and transfer of small Li^+ ions in the composite cathode would promote the battery capacity and reaction dynamics. In the n-type doping process, Li_3PO_4 can improve the ionic conductivity and thus increase the specific capacity of the composite cathode (Fig. S36†).

$$\begin{aligned}&\text{Charge}: \text{CTF-M} + Li_3PO_4 - xe^- - xLi^+ \\ &\quad \rightarrow \text{CTF-M}^{x+} + Li_{(3-x)}PO_4^{x-} \\ &\text{Discharge}: \text{CTF-M}^{x+} + Li_{(3-x)}PO_4^{x-} + xe^- + xLi^+ \\ &\quad \rightarrow \text{CTF-M} + Li_3PO_4\end{aligned} \quad (1)$$

To further confirm the wide availability of this biphase coupled cathode (BPCC) strategy, the composite cathode comprising Li_3PO_4 and a typical p-type small molecule *N*,*N*,*N*′,*N*′-tetraphenyl-1,4-phenylenediamine (TPPA) was also prepared and found to display an obviously enhanced electrochemical performance compared with a single TPPA cathode and the transformation of the inserted ions from PF_6^- anions to Li^+ cations, further proving that the proposed BPCC strategy has a wide possibility for improving the electrochemical performance of p-type organic cathode materials (Fig. S37 and S38†).

Furthermore, a full cell (CTF-M@Li_3PO_4//CTF-550) was assembled by using CTF-M@Li_3PO_4 composites as the cathode (the weight ratio of CTF-M, ketjen black, and PVDF was 4 : 5 : 1) and CTF-550 as the anode. Fig. 4a shows the rate performance of CTF-M@Li_3PO_4//CTF-550, with an initial discharge specific capacity of 101.2 mA h g^{-1} at 0.2 A g^{-1}, and even at 10 A g^{-1}, the capacity was still 25.1 mA h g^{-1} (Fig. 4b), which was much better than CTF-M//CTF-550 (Fig. S32†). The electrochemical performance of CTF-M@Li_3PO_4 composite electrodes showed significant advantages over the reported p-type organic electrode materials (Table S3†). When the current density returned to 0.2 A g^{-1} again, the capacity was 66.8 mA h g^{-1}. In addition, the coulombic efficiency was also significantly improved compared with that of the CTF-M//CTF-550 battery. The long-term cycling stability of the CTF-M@Li_3PO_4//CTF-550 battery was also investigated as shown in Fig. 4c. At 1 A g^{-1}, the battery showed an initial discharge specific capacity of 54.4 mA h g^{-1}, and after 300 cycles the capacity could maintain at 31.4 mA h g^{-1}, with a coulombic efficiency of above 95%.

As is well known, unlike conventional inorganic lithium-containing oxide cathodes, most organic electrodes cannot provide Li^+ sources when used as the cathode of the lithium-

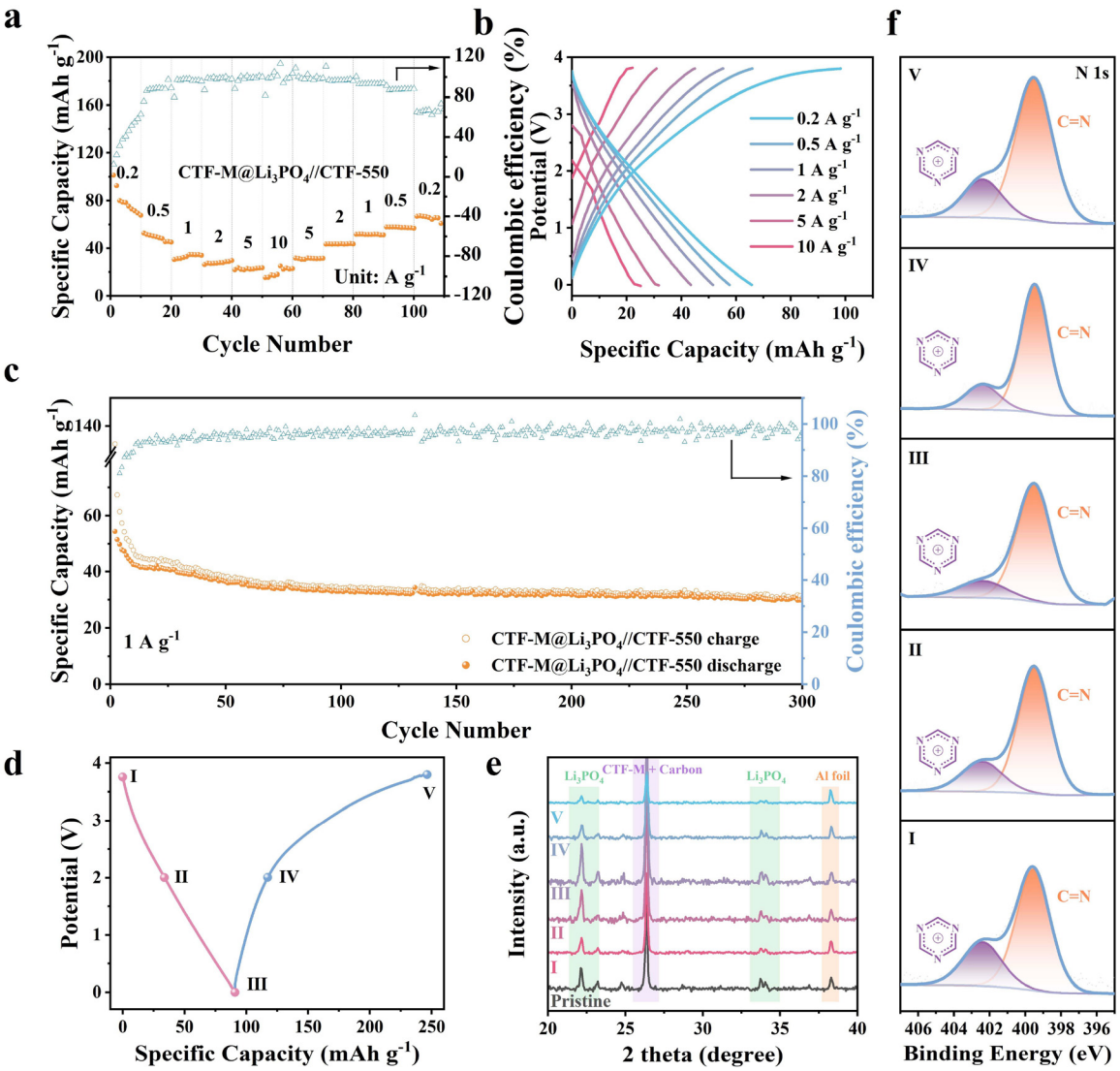

Fig. 4 (a) Rate performance of CTF-M@Li_3PO_4//CTF-550 at various current densities. (b) Charge/discharge curves of CTF-M@Li_3PO_4//CTF-550. (c) Cycling performance of CTF-M@Li_3PO_4//CTF-550 at 1 A g^{-1}. Ex situ characterization of the cathode of CTF-M@Li_3PO_4//CTF-550 at different discharge and charge states: (d) Charge/discharge curves, (e) XRD spectra of the cathode, (f) XPS spectra of N 1s of the cathode.

ion battery and have to pair with lithium metal or a prelithiated anode for normal working, which results in the fact that lithium organic batteries face the challenges from the metal lithium anode or complicated prelithiation operation. In the case of the p-type organic cathode, the insertion/extraction of large anions from electrolytes in the cathode will significantly affect the battery reaction dynamics, and more seriously decrease electrolyte concentration and bring about electrolyte-dependent capacity limit, namely, the anion amount in the electrolyte determines the upper limit of the charge storage capacity. Therefore, to avoid electrolyte dependence of battery capacity, Li_3PO_4 was introduced into the cathode, and the working mode of the full battery changed from that of a dual ion battery to a rocking chair battery. In this work, a CTF-M@Li_3PO_4//CTF-550 battery was employed as the typical example to demonstrate this concept. The reaction processes at the cathode and anode are shown in Fig. 5a and b. During the charging process, active triazine units lost electrons and formed triazine radical cations, while Li_3PO_4 lost Li^+ ions, leaving PO_4^{3-} anions to balance the positive charges of triazine radical cations for achieving a stable charge neutral structure. During the discharge process, the triazine radical units received electrons to restore the original triazine structure, while PO_4^{3-} was again combined with Li^+ to form Li_3PO_4. Briefly, only Li^+ shuttled between the cathode and the anode during the charge and discharge process, and thus the CTF-M@Li_3PO_4//CTF-550 can be considered as an all-organic rocking-chair battery (RCB). The structural changes of Li_3PO_4 and triazine rings during charge and discharge were verified by *ex situ* XRD and *ex situ* XPS. Fig. 4d shows the charge/discharge curves of the cathode in the voltage range of 0 V to 3.8 V at 0.1 A g^{-1}. XRD patterns of the electrodes at different

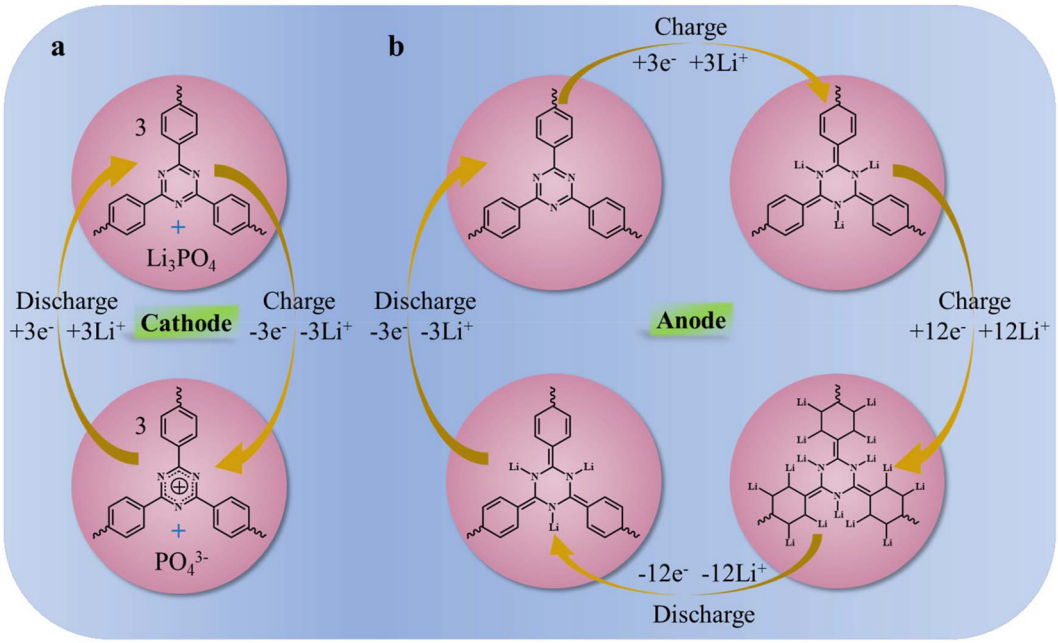

Fig. 5 Charge storage mechanism during the charging and discharging of (a) the cathode and (b) the anode.

charge/discharge stages of the second cycle are shown in Fig. 4e, and it can be seen that the peaks of Li_3PO_4 had gradually weakened in charging up to 3.8 V, and gradually strengthened in discharging down to 0 V, which was consistent with the Li_3PO_4 transformation mechanism proposed in Fig. 5a. It is worth noting that the XRD signals of Li_3PO_4 and CTF-M will disappear gradually with the cycles, suggesting the structural rearrangement of the composite cathode and the formation of a new thermodynamically stable structure (Fig. S40†). The N 1s XPS spectra of the cathode at different charge/discharge stages were also investigated. As shown in Fig. 4f, the peak of the triazine radical cation was enhanced during charging to 3.8 V, and gradually weakened during discharging to 0 V.[23,36,37] All these results well support the proposed lithium storage mechanism of the CTF-M@Li_3PO_4 composite cathode as shown in Fig. 5a. Besides, the Li^+ storage mechanism of the CTF-550 anode is shown in Fig. 5b, and its superb specific capacity should be attributed to the lithium storage of C═N of the triazine rings and C═C of the cyclohexadiene rings derived from benzene rings.[40,46–51]

3. Conclusion

A CTF with an AB stacking structure and excellent crystallinity was synthesized in the $AlCl_3$–NaCl–KCl molten salt system at 180 °C using DCB as the raw material. A series of comparative tests demonstrated that the reaction time, reaction temperature and the ratio of DCB to molten salt have a combined effect on the crystallinity of the CTF. The AB-stacked CTF showed obviously better electrochemical performance than the AA-stacked one and can behave as both the cathode and anode of lithium-ion batteries. Consequently, a rocking chair full cell consisting of the CTFs@Li_3PO_4 cathode and CTF anode was assembled and delivered an initial discharge specific capacity of 101.2 mA h g^{-1} at 0.2 A g^{-1}. *Ex situ* FTIR and XPS tests revealed the reversible Li^+ insertion/extraction at C═N sites of the triazine rings and C═C sites of cyclohexadiene rings for the anode and the synergistic lithium storage of triazine rings and Li_3PO_4 in the cathode. This work demonstrated the possibility of further exploring a low-temperature molten salt system for organic synthesis and filled the gap in the lithium storage study of crystalline AB stacked CTFs. More importantly, we proposed and verified a new-type biphase coupled composite cathode model built using Li_3PO_4 and a p-type organic electrode and enabled a rocking chair organic lithium ion battery beyond a dual ion battery, which will substantially promote the development of high-energy organic energy storage. The concept can also be extended to other organic metal ion batteries.

Author contributions

Conceptualization: X. Y., M. H., and J. Y.; methodology: X. Y., G. Z., C. W., and M. H.; investigation: X. Y., G. Z., C. W., Y. D., J. X., and M. H.; computation: G. Z.; writing – original draft: X. Y. and M. H.; writing – review and editing, X. Y., X. W., H. Y., Z. W., R. L., J. L. and M. H.; M. H. and J. Y. jointly supervised this work.

Date availability statements

The data supporting this article have been included as part of the ESI.†

Conflicts of interest

The authors declare no conflict of interest.

Acknowledgements

We acknowledge the financial support by the National Natural Science Foundation of China (22371010, 21771017 and 51702009), the "Hundred Talents Program" of the Chinese Academy of Science, Fundamental Research Funds for the Central Universities, Shenzhen Science and Technology Program (JCYJ20210324115412035 JCYJ2021-0324123202008, JCYJ20210324122803009 and ZDSYS20210813095534001), and the Guangdong Basic and Applied Basic Research Foundation (2021A1515110880).

References

1 B. Zhang, W. Wang, L. Liang, Z. Xu, X. Li and S. Qiao, *Coord. Chem. Rev.*, 2021, **436**, 213782.
2 J. Xu, J. Mahmood, Y. Dou, S. Dou, F. Li, L. Dai and J. Baek, *Adv. Mater.*, 2017, **29**, 1702007.
3 B. Häupler, A. Wild and U. S. Schubert, *Adv. Energy Mater.*, 2015, **5**, 1402034.
4 T. B. Schon, B. T. McAllister, P.-F. Li and D. S. Seferos, *Chem. Soc. Rev.*, 2016, **45**, 6345–6404.
5 B. Yang, Y. Wang, H. Bian, Y. Zhang, Y. Du, H. Lu and D. Bin, *Chem. Commun.*, 2023, **59**, 8246–8249.
6 W. Zhang, B. Song, M. Wang, T. Miao, X.-L. Huang, E. Zhang, X. Zhan, Y. Yang, H. Zhang and K. Lu, *Energy Environ. Sci.*, 2024, **17**, 5273–5282.
7 S. Wang, Q. Wang, P. Shao, Y. Han, X. Gao, L. Ma, S. Yuan, X. Ma, J. Zhou, X. Feng and B. Wang, *J. Am. Chem. Soc.*, 2017, **139**, 4258–4261.
8 Z. Song and H. Zhou, *Energy Environ. Sci.*, 2013, **6**, 2280–2301.
9 K. Sakaushi, G. Nickerl, F. M. Wisser, D. Nishio-Hamane, E. Hosono, H. Zhou, S. Kaskel and J. Eckert, *Angew. Chem., Int. Ed.*, 2012, **51**, 7850–7854.
10 X. Chen, H. Zhang, P. Yan, B. Liu, X. Cao, C. Zhan, Y. Wang and J.-H. Liu, *RSC Adv.*, 2022, **12**, 11484–11491.
11 Y.-Q. Cai, Z.-T. Gong, Q. Rong, J.-M. Liu, L.-F. Yao, F.-X. Cheng, J.-J. Liu, S.-B. Xia and H. Guo, *Appl. Surf. Sci.*, 2022, **594**, 153481.
12 K. A. See, S. Hug, K. Schwinghammer, M. A. Lumley, Y. Zheng, J. M. Nolt, G. D. Stucky, F. Wudl, B. V. Lotsch and R. Seshadri, *Chem. Mater.*, 2015, **27**, 3821–3829.
13 Y. Zhu, X. Chen, Y. Cao, W. Peng, Y. Li, G. Zhang, F. Zhang and X. Fan, *Chem. Commun.*, 2019, **55**, 1434–1437.
14 T. Zhou, Y. Zhao, J. W. Choi and A. Coskun, *Angew. Chem., Int. Ed.*, 2019, **58**, 16795–16799.
15 X. Zhu, C. Tian, S. M. Mahurin, S.-H. Chai, C. Wang, S. Brown, G. M. Veith, H. Luo, H. Liu and S. Dai, *J. Am. Chem. Soc.*, 2012, **134**, 10478–10484.
16 S. Ren, M. J. Bojdys, R. Dawson, A. Laybourn, Y. Z. Khimyak, D. J. Adams and A. I. Cooper, *Adv. Mater.*, 2012, **24**, 2357–2361.
17 Z.-A. Lan, M. Wu, Z. Fang, Y. Zhang, X. Chen, G. Zhang and X. Wang, *Angew. Chem.*, 2022, **134**, e202201482.
18 P. Kuhn, A. Forget, D. Su, A. Thomas and M. Antonietti, *J. Am. Chem. Soc.*, 2008, **130**, 13333–13337.
19 Q. Pang, J. Meng, S. Gupta, X. Hong, C. Y. Kwok, J. Zhao, Y. Jin, L. Xu, O. Karahan, Z. Wang, S. Toll, L. Mai, L. F. Nazar, M. Balasubramanian, B. Narayanan and D. R. Sadoway, *Nature*, 2022, **608**, 704–711.
20 R. Midorikawa, *Denki Kagaku*, 1955, **23**, 127–129.
21 L. Xiang, X. Ou, X. Wang, Z. Zhou, X. Li and Y. Tang, *Angew. Chem., Int. Ed.*, 2020, **59**, 17924–17930.
22 K. V. Kravchyk and M. V. Kovalenko, *Adv. Energy Mater.*, 2019, **9**, 1901749.
23 Z. Wang, S. Gu, L. Cao, L. Kong, Z. Wang, N. Qin, M. Li, W. Luo, J. Chen, S. Wu, G. Liu, H. Yuan, Y. Bai, K. Zhang and Z. Lu, *ACS Appl. Mater. Interfaces*, 2021, **13**, 514–521.
24 R. Zhang, Z. Liu, T.-N. Gao, L. Zhang, Y. Zheng, J. Zhang, L. Zhang and Z.-A. Qiao, *Angew. Chem., Int. Ed.*, 2021, **60**, 24299–24305.
25 C. Wang, H. Zhang, W. Luo, T. Sun and Y. Xu, *Angew. Chem., Int. Ed.*, 2021, **60**, 25381–25390.
26 Y. Li, R. Zhang, C. Li, H. Li, Q. Fang and T. Xie, *J. Colloid Interface Sci.*, 2022, **608**, 1449–1456.
27 J. Xiong, X. Yan, H. Yu, C. Wu, G. Zhao, J. Zhang, Y. Dai, X. Wang, J. Gao, X. Pu, M. Hu, J. Liu and J. Yang, *J. Mater. Chem. A*, 2023, **11**, 8048–8056.
28 D. Leanza, C. A. F. Vaz, P. Novák and M. El Kazzi, *Helv. Chim. Acta*, 2021, **104**, e2000183.
29 Q. Geng, Z. Xu, J. Wang, C. Song, Y. Wu and Y. Wang, *Chem. Eng. J.*, 2023, **469**, 143941.
30 Y. Wang, X. Zhu, M. Yang, H. Ma, R. Li, J. Zhang, Q. Zhao, J. Ren, X. Wang, H. Yu, J. Gao, M. Hu and J. Yang, *ACS Appl. Mater. Interfaces*, 2023, **15**, 22051–22064.
31 X. Shen, Y. Li, T. Qian, J. Liu, J. Zhou, C. Yan and J. B. Goodenough, *Nat. Commun.*, 2019, **10**, 900.
32 L. Cao, D. Li, T. Pollard, T. Deng, B. Zhang, C. Yang, L. Chen, J. Vatamanu, E. Hu, M. J. Hourwitz, L. Ma, M. Ding, Q. Li, S. Hou, K. Gaskell, J. T. Fourkas, X.-Q. Yang, K. Xu, O. Borodin and C. Wang, *Nat. Nanotechnol.*, 2021, **16**, 902–910.
33 S. Tan, Y. Jiang, S. Ni, H. Wang, F. Xiong, L. Cui, X. Pan, C. Tang, Y. Rong, Q. An and L. Mai, *Natl. Sci. Rev.*, 2022, **9**, nwac183.
34 S. Zhang, G. Cheng, L. Guo, N. Wang, B. Tan and S. Jin, *Angew. Chem., Int. Ed.*, 2020, **59**, 6007–6014.
35 Y. Zhu, M. Qiao, W. Peng, Y. Li, G. Zhang, F. Zhang, Y. Li and X. Fan, *J. Mater. Chem. A*, 2017, **5**, 9272–9278.
36 Y. Dai, W. Li, Z. Chen, X. Zhu, J. Liu, R. Zhao, D. S. Wright, A. Noori, M. F. Mousavi and C. Zhang, *J. Mater. Chem. A*, 2019, **7**, 16397–16405.

37 J. Huang, S. Hu, X. Yuan, Z. Xiang, M. Huang, K. Wan, J. Piao, Z. Fu and Z. Liang, *Angew. Chem., Int. Ed.*, 2021, **60**, 20921–20925.
38 F. Jiang, Y. Wang, T. Qiu, Y. Zhang, W. Zhu, C. Yang, J. Huang, Z. Fang and G. Dai, *ACS Appl. Mater. Interfaces*, 2021, **13**, 48818–48827.
39 Y. Wang, X. Li, L. Chen, Z. Xiong, J. Feng, L. Zhao, Z. Wang and Y. Zhao, *Carbon*, 2019, **155**, 445–452.
40 Z. Lei, Q. Yang, Y. Xu, S. Guo, W. Sun, H. Liu, L.-P. Lv, Y. Zhang and Y. Wang, *Nat. Commun.*, 2018, **9**, 576.
41 X. Han, G. Qing, J. Sun and T. Sun, *Angew. Chem., Int. Ed.*, 2012, **51**, 5147–5151.
42 J. Yu, N. Li, H. Wang, B. Gao, B. Wang and Z. Li, *Chem. Eng. J.*, 2023, **463**, 142434.
43 S. Chen, S. Wang, X. Xue, J. Zhao and H. Du, *Polymers*, 2021, **13**, 3300.
44 K. Sakaushi, E. Hosono, G. Nickerl, T. Gemming, H. Zhou, S. Kaskel and J. Eckert, *Nat. Commun.*, 2013, **4**, 1485.
45 K. Sakaushi, G. Nickerl, F. M. Wisser, D. Nishio-Hamane, E. Hosono, H. Zhou, S. Kaskel and J. Eckert, *Angew. Chem., Int. Ed.*, 2012, **51**, 7850–7854.
46 X. Han, G. Qing, J. Sun and T. Sun, *Angew. Chem., Int. Ed.*, 2023, **51**, 5147–5151.
47 F. Jiang, Y. Wang, T. Qiu, G. Yang, C. Yang, J. Huang, Z. Fang and J. Li, *J. Power Sources*, 2022, **523**, 231041.
48 N. Jiang, M. Qi, Y. Jiang, Y. Fan, S. Jin and Y. Yang, *Energy Environ. Mater.*, 2024, e12797.
49 S.-B. Ren, W. Ma, C. Zhang, L. Chen, K. Wang, R.-R. Li, M. Shen, D.-M. Han, Y. Chen and J.-X. Jiang, *ChemSusChem*, 2020, **13**, 2295–2302.
50 Z. Ba, Z. Wang, Y. Zhou, H. Li, J. Dong, Q. Zhang and X. Zhao, *ACS Appl. Energy Mater.*, 2021, **4**, 13161–13171.
51 Z. Lei, X. Chen, W. Sun, Y. Zhang and Y. Wang, *Adv. Energy Mater.*, 2019, **9**, 1801010.